Numerical and experimental comparative performance analysis of emerging spherical-caged drones

K. Edgerton [a], G. Throneberry [a], A. Takeshita [a], C.M. Hocut [b], F. Shu [a], A. Abdelkefi [a,*]

[a] *Department of Mechanical and Aerospace Engineering, New Mexico State University, Las Cruces, NM 88003, USA*
[b] *CCDC Army Research Laboratory, White Sands Missile Range, New Mexico 88002, USA*

A B S T R A C T

As technology in the 21st century matures at a faster pace, one technology is taking major strides as an everyday utility: unmanned aerial vehicles. Spherical drones are an emerging technology to tackle environments that previous systems have had considerable trouble trying to navigate in. These systems have equal potential in both military and civilian applications. A spherical cage is designed for a traditional pusher quad-copter and fabricated out of low-cost 3D-printer materials including polylactic acid (PLA) and acrylonitrile butadiene styrene (ABS). Autodesk Finite Element Analysis simulations are carried out to show stress and performance relations for the various material densities. Endurance and thrust to weight considerations are tested to further optimize the low-cost vehicle utilizing New Mexico State University's (NMSU) wind tunnel. The vehicle is also mounted to a thrust test stand from RCBenchmark that can measure RPM, power consumption, thrust, and torque. The effect of cage interference is compared with changing airflow interference so that different cage platforms can be installed for mission sets that require more protected or gapped configurations. Although every airframe will have slight changes in the methodology used for design, this reliable strategy can be the framework for future spherical drone prototyping.

1. Introduction

The increased utilization of drones has led to rapid development in technology. The number of applications drones are being used for is rapidly increasing and is starting to branch into low altitude or underground areas, and high-risk environments where there are foreign objects that present collision hazards. These high-risk environments (forests, glaciers, tunnels, mountainsides, and more) often lack the external navigational aids, such as orbiting satellites or terrestrial antennae for rapid vector changes. A vehicle in this mission set needs to be able to navigate without having access to these low latency inputs. Uses of this drone type can easily grow and expand into roles that traditional rotorcraft are being optimized for such as organ transplant, disease control, and package delivery [1–8]. Studies focusing on law enforcement application have great potential as well [9]. The major obstacle spherical vehicles are combating is the torque experienced by the vehicle during a collision and the normal force of the colliding material. Other fixed caged systems on previous vehicles that are fixed in

place, protect the user of the drone and the vehicle, however, not the mission in its entirety. Fixed protective measures around the power plant, such as propeller guards are only a planar defense. It is highly desirable to have comprehensive protection.

This study is not the first attempt at enclosing a drone in a passive system, therefore the objectives of the study are to present a design methodology and outline key design choices that need to be made in the development of caged systems. Previous research and industry attempts have developed mature and capable systems but the methodology for rapid, yet effective experimentation differs. A few previous successful examples and research comparisons of these vehicles are briefly described in this section. The proposed uses also vary greatly from search and rescue, infrastructure analysis, and even sports improvement programs [10]. One commercial vehicle that takes advantage of a rectangular cage to protect itself is the Passport. Available on Amazon and other easily accessible vendors, its portability and marketability are centered on its foldable structure. Passport is either folded for transport or rotated into a flyable orientation. Four motors, each with a 3-bladed propeller give this VHS sized vehicle the ability to take photos for drone enthusiasts. Given the cage's hatch cross-linked members, it would be very difficult for someone to harm themselves while

Fig. 1. Flyability spherical drone.

deploying the vehicle by hand. Although an incredibly important feature, this fixed rectangular system cannot reduce torque during a collision and it is almost certain that the rectangular geometry will inhibit swift recoveries after collisions by the vehicle itself. Moving to spherical designs, Fleye has recently taken flight with the assistance of Kickstarter promised funding orders. Based on an injection molded plastic case, the vehicle is powered by a single relatively powerful ducted fan unit. Sold for drone pilot training and event documentation, Fleye's strengths are similar to the Passport but include an increased flight time of almost 20 minutes [11–13]. It protects the user and the vehicle in assisted take-offs and simple collision events. Similar to the Passport though, the cage is fixed in place. When storage and protection are coupled, other researchers, such as Kornatowski et al. [14] have proposed an origami drone that solves this issue better than Passport. Built for package delivery and the explicit protection of the user, this vehicle can be folded down to 92% of its original volume when the mission is complete.

When ground locomotion and inspection come to the forefront of the drone design, other designs have been researched as well. Some researchers started with the spherical design while others acknowledge that a cylindrical vehicle will promote ground stability. Yamada et al. [15] researched and tested a drone that rotates within its cylindrical protective structure for the purpose of infrastructure analysis. Air resistance of the cage also is taken into consideration as it would negatively impact endurance. The undeniable industry leader in the field of rotating spherical systems is the private company Flyability [16] based in Switzerland. Their system has the flight endurance of typical uncaged systems while featuring a fully encapsulated protective system. As can be seen in Fig. 1, their design utilizes a compact multi-rotor configuration and dense fuselage with 3-axis rotation to ensure there is minimal effect on vehicle from torque after a collision. Other previous studies including Mizutani et al. [17] have focused on the cage geometry and interaction with a commercially integrated vehicle as it rotates.

This study is focused on the integration of a passive protective mechanism consisting of a rotating additively manufactured cage on a multi-rotor drone that is designed to be able to rotate in 3-dimensions around the drone with the help of bearings. The cage will protect the vehicle as it traverses obstacle dense environments that could lead to collisions. It is important to note that this scalable study could aid in the design of spherical cages multi-rotor systems of multiple size and motor configurations. This study is aimed at extensively studying the design methodology of caged, spherical drones and to provide insight on the important design parameters and improvements that can be made to current and

future spherical drone technologies. This study includes analytical modeling, finite element simulations to investigate the structural characteristics of the system, and aerodynamic studies to explore the impact of the cage and drone body on system performance. In Section 2, the analytical and numerical modeling are presented, followed by finite element analysis for the cage and the propellers in Section 3. Aerodynamic investigations using wind tunnel testing, to include smoke visualization and particle image velocimetry, are presented in Section 4. In Section 5, prototyping and flight testing are presented, and finally conclusions are provided in Section 6.

2. Analytical and numerical modeling of spherical system

In the design of a passive protective cage, material properties of the cage, such as hardness, rigidity, coarseness, flexibility, and even layer adhesion (if 3D printed) must be considered, however, the model of the protective structure can be simplified to that of a ball colliding with local obstacles. To do this, coefficients of restitution in the horizontal, e_x and the vertical e_y directions are used to study a range of collisions. The coefficients of restitution are expressed as follows:

$$e_y = -\frac{V_{y2}}{V_{y1}} \tag{1}$$

$$e_x = -\frac{(V_{x2} - R\omega_2)}{(V_{x1} - R\omega_1)} \tag{2}$$

The cage itself can be modeled as a thin spherical sphere. For the development of a theoretical model, the coefficients of restitution are broken down into their respective X and Y components which reduces the need to analyze the foreign objects coefficients of friction in infinite directions as the results are only in the X and Y directions, respectively. Fig. 2 provides a schematic of the collision of a fixed protective cage system with a surface.

In the event of a frictionless collision event (i.e. the coefficients of both static and dynamic friction are zero), the cage will have similar properties mirrored across the collision. An exact mirroring of properties would mean that the cage conserves all of its elastic potential energy such that the pre- and post-collision angular and linear velocity are conserved, and $\theta_1 = \theta_2$. Assuming that the cage receives no additional energy from the horizontal surface, as can be inferred from equation (1), the range of e_y is finite with a maximum magnitude of 1 [18]. Ranging from 0 to 1, this coefficient provides the momentum (no mass change during the event) or velocity changes for the cage during the collision. A value of 0 represents a case where the cage does not leave the surface after the collision and carries no momentum and a value of 1 represents a case where the cage carries all energy it possessed prior to the collision.

As the Y component of the coefficient of restitution defines the properties of the ball, a coefficient is needed to define the properties of the colliding surface interacting with the ball. This coefficient is a dimensionless value displaying how the surface affects the angular and translational energies. The angular values are subtracted as they represent a counterclockwise motion against the linear motion. The coefficient in the X direction, e_x, defines the properties of the colliding cage that interacts with the foreign object. Shifts of angular and translational energies represent friction in a non-dimensional value. The value of e_x ranges between -1 to 1, where the lowest value of -1 represents a frictionless surface while an upper value of 1 represents a collision that changes both angular and translation velocities signs.

To find the post-collision angular and translational velocities from equation (2), the vehicle parameters must be known and it is advantageous to derive an equation with only pre-collision parameters as Cross [19] has done for a colliding ball which relates the
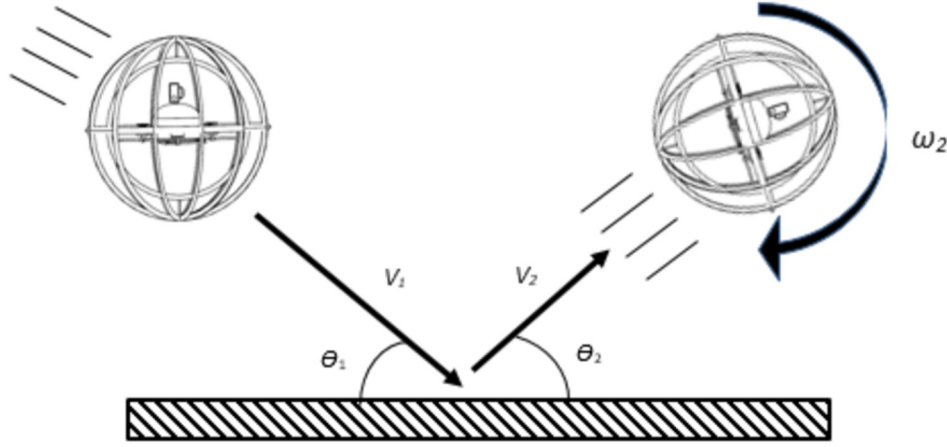
Fig. 2. Collision with a fixed cage system.

Table 1
Dynamical modeling parameters.

V_{x1}	Pre-collision x-velocity
V_{y1}	Pre-collision y-velocity
V_{x2}	Post-collision x-velocity
V_{y2}	Post-collision y-velocity
ω_1	Pre-collision angular velocity
ω_2	Post-collision angular velocity
R	Cage radius
I	Moment of inertia of cage
A	Inertial coefficient
M	System mass
e_x	x-coefficient of restitution
e_y	y-coefficient of restitution

Table 2
Post-collision velocity and force equations.

I	II
$\omega_2 = \frac{V_{x2} + e_x(V_{x1} - R\omega_1)}{1 + \alpha}$	$V_{x2} = \frac{V_{x1}(1 - \alpha e_x)}{\alpha + 1}$
III	**IV**
$F_x = \frac{mV_{x1}\alpha(e_x + 1)}{\Delta t(\alpha + 1)}$	$F_y = \frac{-mV_{y1}(e_y + 1)}{\Delta t}$

conservation of momentum as shown in equations (3), (4), and (5), where equation (3) is the post-collision translational velocity and equation (4) is the conservation of momentum. The parameters provided in Table 1 are used throughout the dynamical modeling.

The post-collision translational velocity in equations (3) and (4) can be used to obtain the post-collision angular velocity as seen in Table 2. Similarly, a post-collision linear velocity equation comprised of only pre-collision parameters can be obtained from the angular velocity in equations (3) and (5), and is shown in Table 2.

$$V_{x2} = -e_x(V_{x1} - R\omega_1) + R\omega_2 \tag{3}$$

$$I\omega_1 + mRV_{x1} = I\omega_2 + mRV_{x2} \tag{4}$$

$$V_{x2} = \frac{\alpha mR^2\omega_1 + mRV_{x1} - \alpha mR^2\omega_2}{mR} \tag{5}$$

Lastly, the forces during the collisions are needed to accurately simulate the collision. The horizontal force integrated with time is equal to the change in momentum during the collision as shown in equations (6) and (7). A similar expression can be derived for the normal force as shown in equations (8) and (9).

$$\int F dt = m\Delta v_x \tag{6}$$

$$F\Delta t = m(V_{x2} - V_{x1}) \tag{7}$$

$$\int N dt = m\Delta v_y \tag{8}$$

$$F_y \Delta t = m(V_{y2} - V_{y1}) \tag{9}$$

The horizontal and normal forces shown in Table 2 are then obtained using equations (1), (7), and (9).

In Fig. 3, experimental results for two scenarios, a ball being dropped on a 20° and a 45° angled surface, from Cross [19] are compared to the model described above. The dashed black line

shows the change in angles of collision ratio and its increase can be attributed to the higher sliding coefficient value creating more friction. The solid red line, depicting the velocity ratio, shows a decrease due to the increased friction. The dotted blue line shows the transfer of linear to radial velocity as the ball grips the surface quicker as the coefficient of sliding friction is increased. For both Figs. 3(a) and 3(b), there is a point where all constants plateau and become constant. This point is where the coefficient of sliding friction exceeds the other isolated parameters.

To help visualize the coupled parameters of interest including time of impact, coefficients of restitution, and horizontal and normal forces, Fig. 4 shows the variations of the horizontal and normal forces with respect to the coefficients of restitution and impact time duration based on Flyability's earlier Gimbal collision tests [18]. Clearly, the coefficients of restitution and time of impact duration highly affect the forces for both scenarios. To encompass a full range of possible outcomes, regardless of the elastic properties $[0 < e_y < 1]$ or frictional properties $[-1 < e_x < 1]$, the cage is subjected to the forces representing the most rigid collision and highest frictional properties for reliable prototyping. An inertial coefficient of $\alpha = 0.9654$ is used as initial CAD thicknesses, proved to be a realistic value. The worst-case collision for friction is represented for a collision of 0.04 seconds and a coefficient of restitution, e_x of 1 in which the frictional force is 15 N, while the upper limit of the normal force is 30 N which occurs for a simulated vertical impact at 3 m/s. The mass is directly proportional to the force as shown in Table 2, so the Finite Element Analysis (FEA) simulations of a 1 kg drone will apply a 150 N normal force.

To determine how the translational velocity is impacted by varying cage thickness, it is essential to consider how the leading inertia coefficient α which is a multiplier of the rotational moment of inertia, affects the speed after collision. The leading inertia coefficients of a cage of uniform 10 mm × 10 mm cross sectional area and constant weight that has a radius that varies between 0.1–0.225 m are shown in Table 3.

The variations of the post-collision linear velocity as a function of the inertial coefficients and horizontal coefficient of restitution are shown in Fig. 5(a). For values of $e_x < 0$, a negligible effect on the post-collision linear velocity is observed while for $e_x = 0$, there
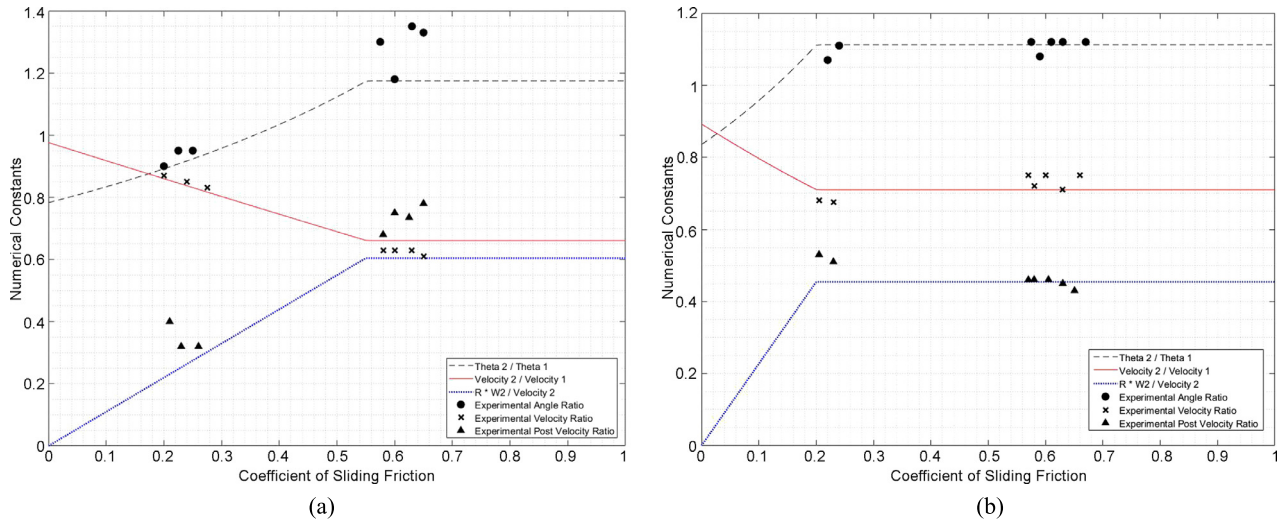
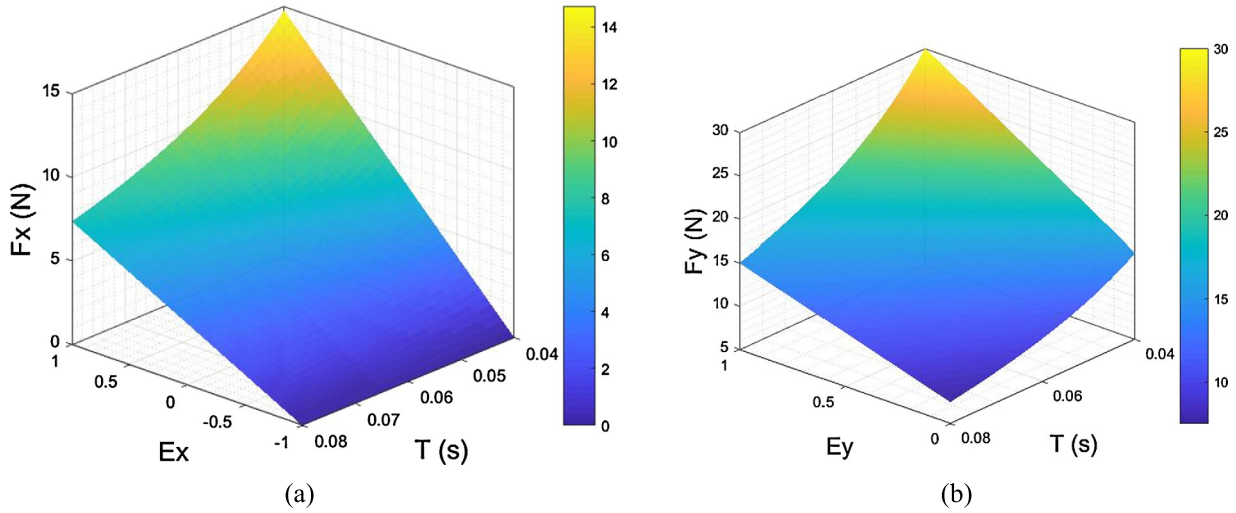**Fig. 3.** Cross coefficient drop test thin walled numerical results at (a) 20° and (b) 45° [19].

Fig. 4. (a) Horizontal forces due to friction and (b) normal forces due to a 0.2 kg cage with radius of 0.225 m. (For interpretation of the colors in the figure(s), the reader is referred to the web version of this article.)

Table 3
Changing inertial coefficients.

Radius	0.10 m	0.15 m	0.18 m	0.20 m	0.23 m
A	0.905	0.923	0.934	0.951	0.965

is a 5.1% difference in velocities for $0.9 < \alpha < 1.0$. At low speeds of ~3 m/s where this study is focused, α can affect the post-collision linear velocity, particularly for $e_x > 0$. Fig. 5(b) shows how a small change in velocity can significantly impact the frictional forces experienced by the cage where a 0.1 m/s increment for the time of duration of the impact causes the cages outer surface to experience a change in forces of 0.25–0.5 N. Therefore, a reduction in the inertial coefficient results in a reduction of the forces experienced by collision-based forces which is especially important for vehicle control and survivability, thus the normal forces will guide the following section's simulations. Changes with inputs of equations II and III from Table 2 are highlighted in Figs. 4(a) and 4(b).

3. Finite element analysis

Survivability and deflection are the two main concerns for cage structural design that plague the traditional spherical system. The main function of the cage (besides ease of ground-based trans-lational movement) is to maintain the drone's integrity during the mission. If the cage cannot withstand the impact or deflections such that it interferes with internal components of itself, the design is unacceptable. To investigate both concerns, two simplified models are designed and subjected to virtual forces to test their mission capabilities. The models both are representative of a simple three orthogonal ring design which is a simple yet effective cage for spherical drones where the spine of the vehicle is intended to sustain the majority of the forces in a collision. In addition, this design has high merits of ease of manufacturability and core strength and it is can be reinforced with more cross members to protect the drone for both higher speed missions and in areas with more protruding foreign objects like forests and collapsed structures. An example of a denser 300-gram cage structure is shown in Fig. 6(a).

Within the cross of the orthogonal rings, there are very small fillets that connect the four spars. The radius of these fillets is 0.4 mm and is representative of the most common 3D printer nozzle. The entire cage could be evaluated for stress using finite element analysis (FEA), however this would require very high element counts with this small radius on all six crosses. To alleviate this issue, the force applied in a worst-case scenario on a single cross at the top of the vehicle will be evaluated with FEA, as shown in
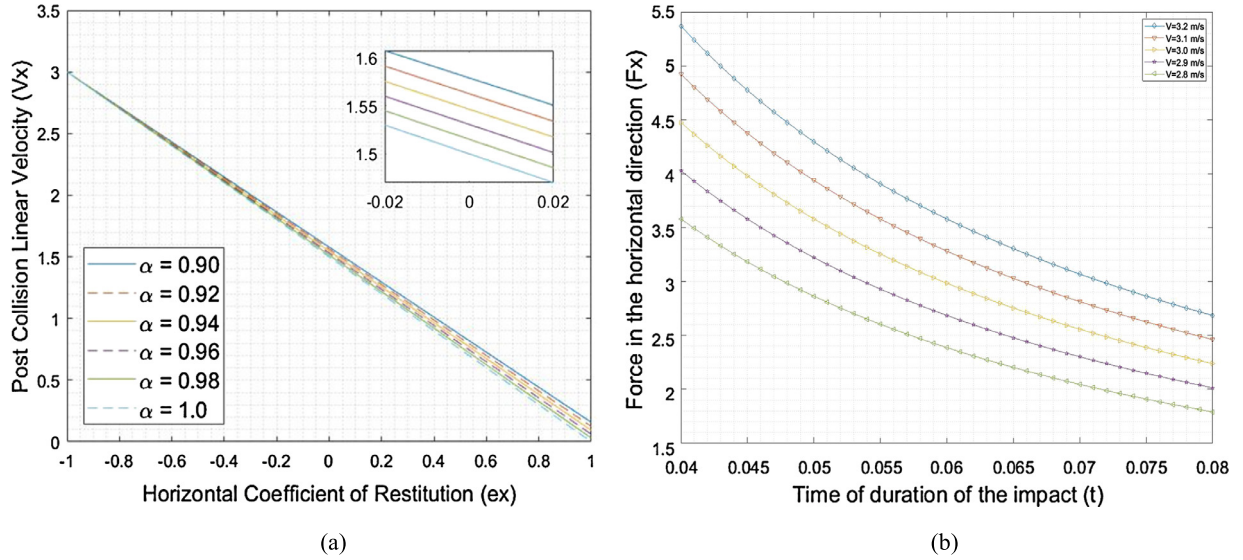
(a)   (b)

Fig. 5. (a) Post-collision translational velocities as a function of α and (b) horizontal force as a function of cage velocity and duration of impact.

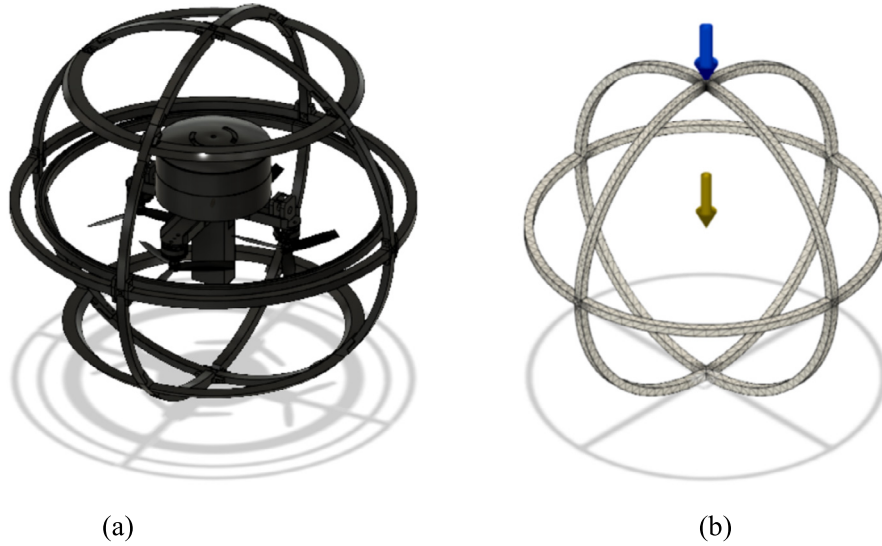(a)   (b)

Fig. 6. (a) 300-gram cage and integrated vehicle and (b) 200-gram meshed cage with an applied 150 N force.

Fig. 7(b) using Autodesk® Fusion 360. The material FEA input properties are gathered from 3D printing and ASME standard tensile tests [20,21]. One major problem with 3D printed materials is that they do not act isotropically, primarily because of the orientation of the printed layers, the possibility that the layers do not adhere properly, and the possibility that a part has a reduced infill ratio to save weight which causes it to exhibit hollow characteristics.

The stress-strain curves from previous research [20,21] show that 20% infill parts which have lower density have a reduced slope and modulus of elasticity which corresponds to a lower stiffness. Simulated impacts of the cage with no vehicle inside are first carried out in which a 150 N is applied to the top of the cage and constraints are applied so that the cage deflects as it would during an impact. Since the materials have a highly nonlinear curve, a convergence analysis is run for both stress and displacement. Since the maximum stress can change between similar models with peak forces, an averaged point probe across the surface is tested as well as maximum forces. For stress, the model converges at 40,000 elements. Similarly, maximum displacement is tested across the ranging element values to see that it converges sooner. For repeatable

and accurate simulations, 40,000 elements are used. The cages are tested in the following order for both stress and displacement: PLA full, ABS full, PLA 20% infill, and the results are shown in Figs. 7 and 8.

This FEA results show that there are significant stress and displacement (especially with the semi-hollow PLA) values that must be considered in the design process. First analyzing the stress, the maximum obtained value exceeds the hollow stress-strain curves which indicates that it is very likely that portions of the cage will crack or fail given high horizontal coefficients of restitution and low impact time collisions. It is likely that the drone would survive the impact, however, it would be unable to endure a second impact of the same magnitude. The displacement results during impact of a 1 kg drone with integrated sensors indicate that the vehicle would require a spacing of nearly 19 mm on each side in order for internal rotation to continue. For such a large deflection, it is important to consider vehicle fabrication methods which produce a more compact vehicle. Only the 20% PLA, 150 N collisions result in complete failure due to the maximum stress exceeds the material strength in which cage replacement would be necessary after
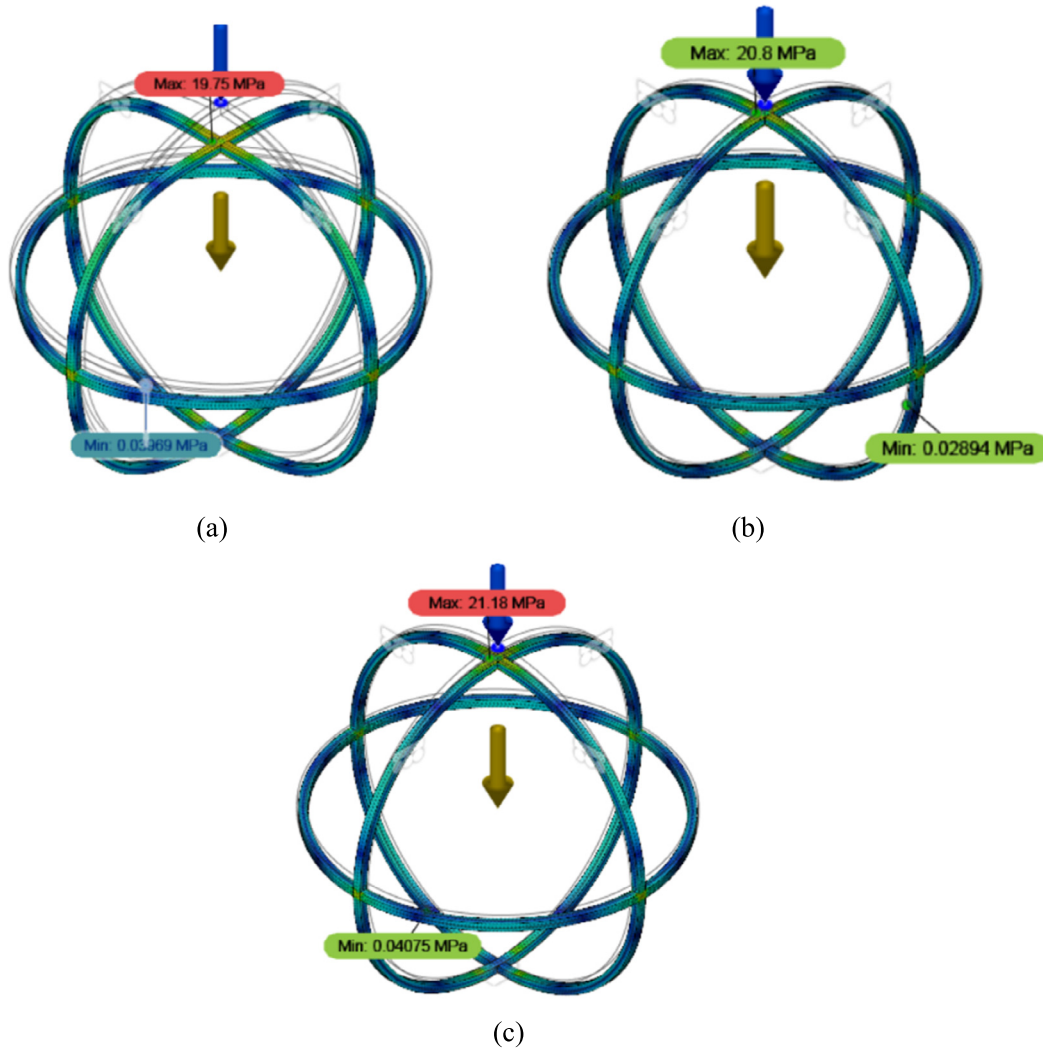
(a)

(b)

(c)

Fig. 7. Cage cross member stress under 150 N normal force for (a) PLA, (b) ABS, and (c) 20% infill PLA.

the mission. Table 4 summarizes the FEA results and the drone's survivability.

The FEA displacement results provide motivation for the production of a compact vehicle in an effort to allow displacement of the cage without propeller interference. As the system becomes more compact, the integration of a powerful power plant with relatively large diameter propellers is difficult due to the cage and drone's geometry. To overcome this limitation, one strategy is to overlap the propeller arcs to decrease the components spacing. This study focuses on overlapping multiple motors instead of coaxial blades to reduce complexity and weight [22,23], although there will be slight reductions in motor efficiency [24]. For this strategy to work, an FEA study is carried out to determine the maximum propeller deflection as a function of the propeller revolutions per minute (RPM).

It is known that multi-rotors have an advantage over traditional rotorcraft as the blades are structurally easier to make with the weight of the craft shared over the four rotors [25]. The material in this study is polycarbonate as many propeller brands use it for the majority of their product [26]. This simulation takes advantage of Fusion 360's linear simulations as polycarbonate is a built-in material and a large portion of its stress-strain curve is linear and it has a higher modulus of elasticity than its additively manufactured based peers [27]. The loading and constraining of the propeller is much different than the point force which was previously applied

Table 4
Summary of FEA stress and displacement results based on materials.

Material	Force applied (N)	Stress (MPa)	Displacement (mm)	Status
PLA	30	4.1	1.9	Survive
ABS	30	4.0	2.56	Survive
PLA (20%)	30	4.1	7.3	Survive
PLA	150	19.8	9.5	Survive
ABS	150	20.8	13.1	Survive
PLA (20%)	150	21.2	47.7	Survive (cage replacement)

to the cage cross member. To find the angular loadings that the propellers experience from high rotational speeds, an RPM sensor is used which measures the change in polarity coming from the electronic speed controller (ESC) to determine the change in the propeller's rotation. A test motor is mounted to an RCBenchmark 1580 thrust test stand to determine the RPM for hovering for two and three blade propellers 17,850 and 13,075, respectively. The linear and angular loading applied are summarized in Table 5. The FEA displacement results of the rotating propellers during hover are shown Figs. 9 and 10 in which the propeller displacements can be as high as 5.5 mm for three blade propellers. These results will serve as guidance to ensure that during rapid motor ramping and vehicle accelerations the propellers can have a local proximity to one another and not strike.
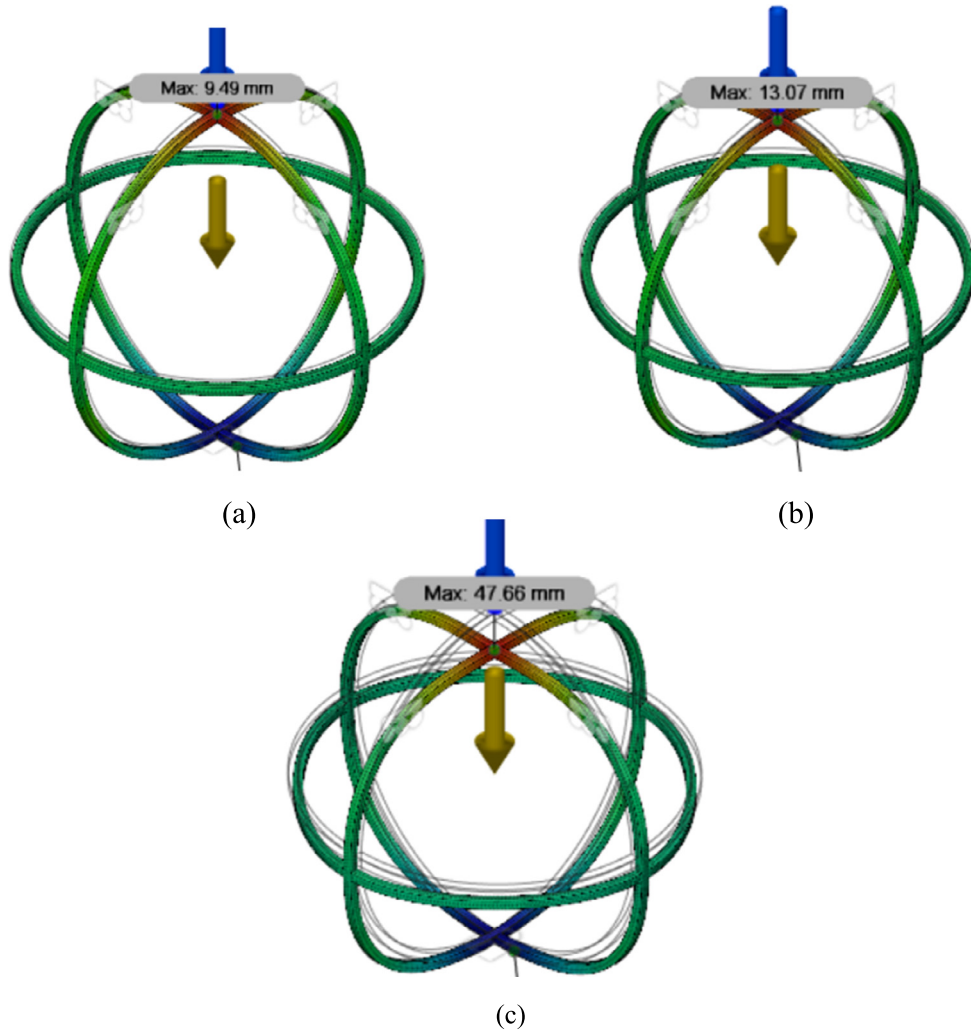
Fig. 8. Cage cross member deflection under 150 N normal force for (a) PLA, (b) ABS, and (c) 20% infill PLA.

Table 5
Overlapping propeller study summary.

Propeller type	Mass (g)	Angular load (deg/s)	Linear load (m/s^2)	Deflection (mm)	Recommended spacing (mm)
2-Blade	3.8	78,450	644.7	2.6	4.0
2-Blade	3.8	107,100	644.7	1.9	3.0
3-Blade	5.2	78,450	471.2	0.8	2.0
3-Blade	5.2	107,100	471.2	5.5	6.5

4. Wind tunnel and thrust test stand analysis

To study the aerodynamic impact of the cage, NMSU's wind tunnel shown in Fig. 11(a) that has a 1.2 × 1.2 m cross section is used for qualitative and quantitative testing. First, flow visualization is carried out using smoke streamlines that are generated from propylene glycol. The smoke is illuminated using a (532 nm, 200 mW) continuous laser equipped with a 60-degree Powell lens. 3D printed mounts are used to mount the vehicle to a vertical cylinder in the test section (Fig. 11(b)) while a 4S 6,600 mAh battery which is mounted to the bottom of the tunnel to decrease flow disturbance is utilized for long endurance tests. The previously used RPM sensor is utilized to determine when the vehicle is below, at, or above the required thrust to represent hovering conditions in the tunnel while the wing tunnel velocity varied between 0–1.7 m/s.
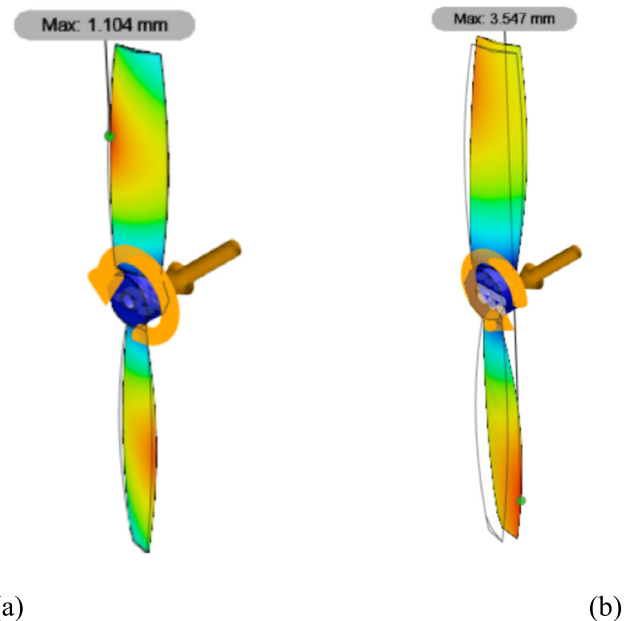

Fig. 9. Two blade propeller deflection during hover for (a) 13,075 RPM and (b) 17,850 RPM.
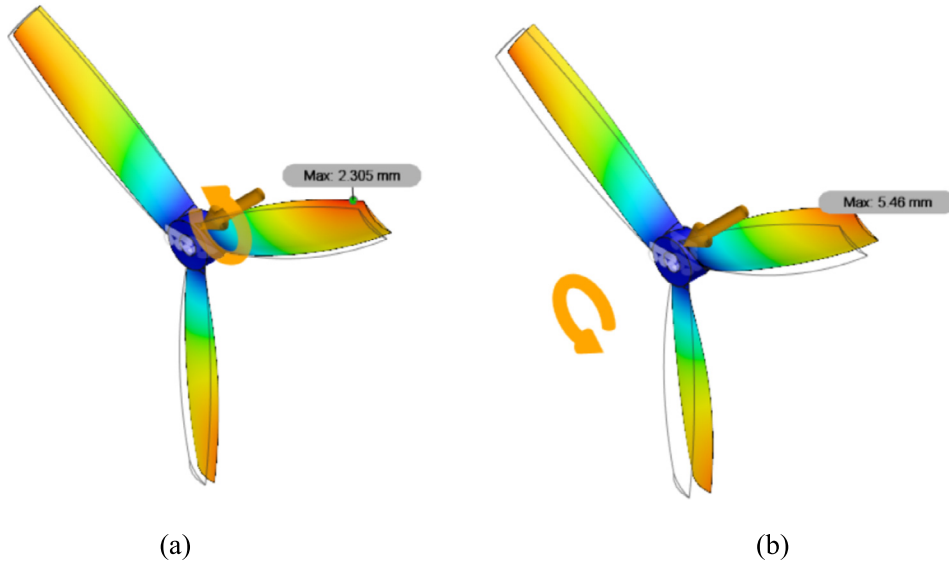
Fig. 10. Three blade propeller deflection during hover for (a) 13,075 RPM and (b) 17,850 RPM.
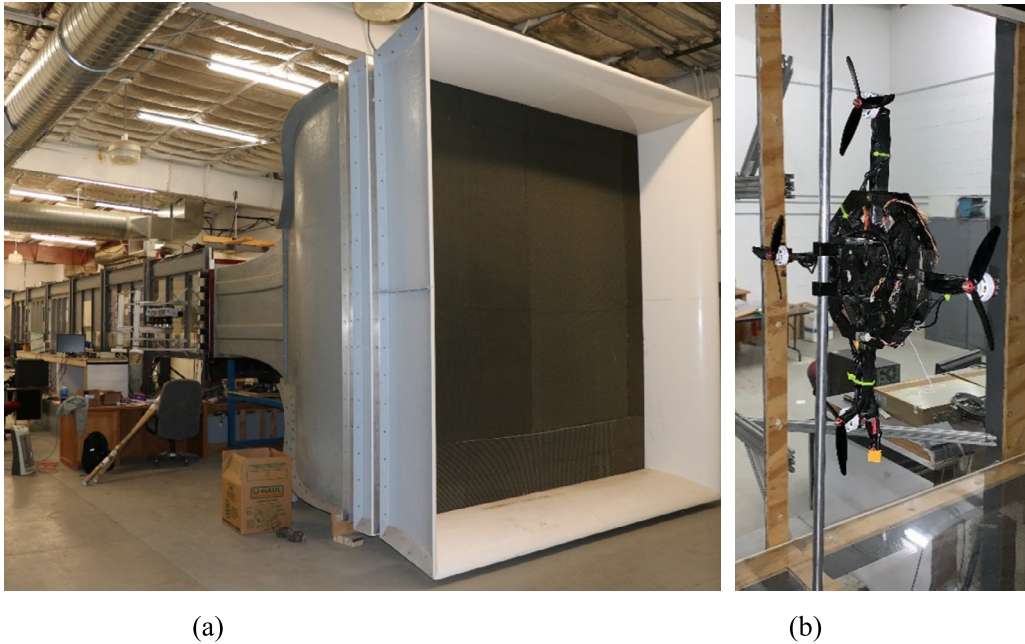

Fig. 11. (a) NMSU low-speed wind tunnel and (b) vertically mounted vehicle in test section for testing.

Fig. 12 shows a still image taken from high speed video of the flow visualization in which the flow is traveling from right to left as indicated by arrows, while the vertical cylinder which stabilizes the drone and the black cage is stark in contrast to the illuminated smoke. The flow has little aerodynamic interaction with the cage for all of the tested cage densities (under zero motor thrust) and flow velocities, as shown in Fig. 12 which is a flow visualization of the highest density cage at a 1.7 m/s velocity, with the exception of small regions of recirculation in the vicinity of the cage cross member, shown in the boxed region in the figure.

A commercial time-resolved Particle Image Velocimetry (PIV) system was used for quantitative tests where the PIV field of view (FOV) was located upstream from the drone and integrated cage, vertically offset 30 mm below the cage centerline. The processed vector field for the previous configuration (0.3 kg, 0.42 m diameter cage at 1.7 m/s freestream velocity) is shown in Fig. 13. The plotted curves in Fig. 14 show the horizontal profiles of the upstream u and v velocity in the vicinity of the caged drone. As the flow approaches the cage, the cage 10 mm × 10 mm cross sections impact the upstream flow up to six thicknesses away from the leading portion of the cage (a black cross is seen in the figure), as a u component velocity deficit of 10% is observed and a v component deviation from freestream is observed. Based on these results, it is clear that in the absence of the motor thrust, the drag due to the cage is minimal.

Fig. 15 shows a still image taken from the flow visualization of the caged drone with the densest cage configuration with the motors spinning to replicate a hovering condition. Upon first glance, it seems that the cage is having a high impact on the flow, however, the flow distortion is actually due to the redirection of the flow around the body of the drone in which there is substantial interaction with the fuselage as the flow reaches the inlet of each propeller. This shows the necessity for the optimization of the incoming flow around the fuselage to enhance motor efficiency. For

Fig. 12. Smoke visualization of 0.3 kg caged drone under zero motor thrust at 1.7 m/s freestream velocity.
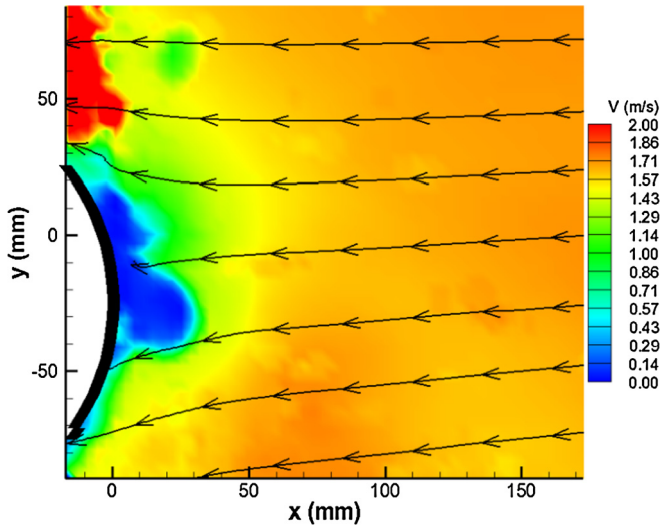

Fig. 13. Streamline results of the interaction of the 0.3 kg caged drone under no motor at 1.7 m/s freestream velocity.

systems that have flap-based control around a single motor [28], this would have major control effects as well.

To quantitatively measure the effects that combined rotor interactions with the fuselage are having on the spherical-caged drone, a thrust stand is utilized to determine the inefficiencies [2,3,29]. Two sets of curves representing data for thrust inefficiencies due to cage interactions and motor and body interactions are shown in Fig. 16. The upper set of thrust curves represents the thrust values for an uncaged and fully 0.3 kg caged version of the vehicle while the propeller RPM is varied over a range similar to studies done on Phantom 3 and other commercial vehicles [30–32]. As expected, the maximum thrust occurs without a cage where there is no parasitic drag on the outflow of the motors. As the propellers are spun up to over 8,000 RPM, the thrust diverges as the cage has more interaction with the incoming thrust, reaching a maximum efficiency

loss of 6.4% at a RPM of 8,300. During rapid horizontal and vertical accelerations, this value would be even higher. Although the drag from translational cage movement with the ambient air does not have a large effect, the thrust from the drone propulsion interaction does.

In addition to investigating the drag from the cage, it is necessary to investigate the hindered thrust from the body of the drone. To do so, the uncaged thrust values of the motors are compared to a single standalone motor detached from the drone. The lower set of thrust curves is generated by taking one fourth of the previous uncaged thrust value and comparing it to the thrust developed by a single motor, which shows that a single motor can lose up to 20.4% efficiency from the interactions of the overlapping motors and the "choking" effect of fuselage components above the motors. These results highlight a conclusion that has not been stressed by previous spherical studies, the body of the vehicle can cause more performance issues than the cage. With this realization, the vehicle's design is optimized to keep the upwind area of the motors as open as possible, as depicted in Fig. 17.

5. Prototype fabrication and flight testing

A quadcopter pusher configuration test vehicle is chosen as it has higher thrust over its puller counterpart [33]. The geometry of the cage's mesh is highly dependent on material choice in manufacturing. A smaller cross section thickness, more dense mesh was considered a poor choice for PLA or ABS because of their brittle properties. In addition, the cage mesh for any spherical system is highly dependent on the environment the drone will be operating in. For example, if the drone is operating in a pipeline or building with no protruding obstructions (such as branches), a low density cage mesh is sufficient for system protection. Alternatively, if the drone is operating in a forest environment or something similar, a higher density cage mesh should be used to provide additional protection from protrusions.

This design is easily repeatable for other researchers or designers with commercial off the shelf 3D printers. A 300 × 300 mm printer bed area was used as it is common as of now. This demonstrates the ease of manufacture of this system and the ability for others to develop similar protective systems. The vehicle is designed and fabricated through the help of industry partners in which a 0.42 m cage was printed in 23 separate parts that are connected with 2 mm fasteners. It is necessary to fabricate the system out of many separate parts due to printing bed limitations and in order to maintain simplicity. If one member breaks in flight, this method allows for easy replacement of a single piece so that the system can be returned to operation rapidly. 3D printing is also used for the fuselage as the design can have accurate cuts for wire holes and autopilot mounts. With low infill, the weight is kept to around 0.55 kg. Due to the compact design, the body overlaps with the flow upstream of the motors (even though they are in a pusher configuration), resulting in audible sounds as the air feeding the propellers has to redirect around the body. Flight testing of the vehicle shown in Fig. 18 included subjecting the vehicle to roll, pitch, and yaw impulses. Free from ground effect, the vehicle is stable in hover and easy to fly as observed by others including Zheng et al. [34]. After hovering, the vehicle was tested in a descent collision resulting in translational movement as projected upon landing through the help of the integrated bearings in which the cage freely rotated as it came to a stop as designed. The system was flown for approximately five minutes although a full endurance test was not conducted. Improving overall flight time was not the primary goal of this work. The addition of the cage will certainly have an adverse effect on flight time but as shown in Fig. 16, the thrust efficiency of the caged system is comparable to the uncaged system. The additional weight of the cage will
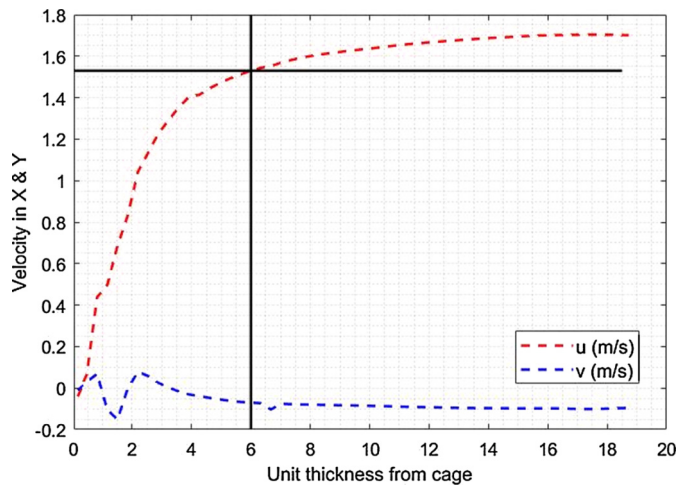
Fig. 14. *u* and *v* velocity component profiles upstream of the caged drone under zero motor thrust.
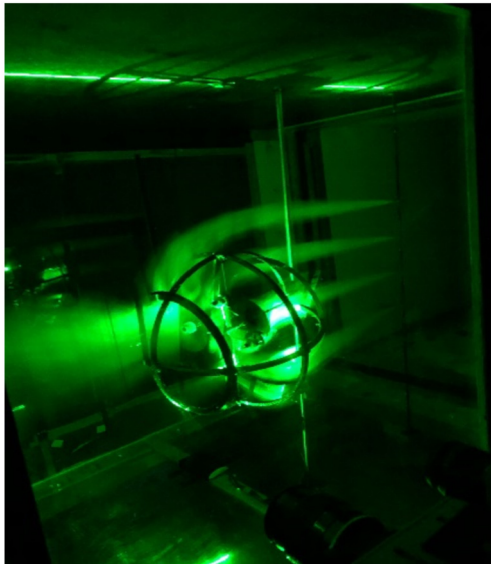

Fig. 16. Thrust inefficiencies of both cage and motor and body interaction.

Fig. 15. Smoke flow visualization of 0.3 kg caged drone at 1.7 m/s freestream velocity under motor thrust.

Fig. 17. Body motor inlet improved vehicle.

also impact the endurance of the system and therefore the weight should be minimized as much as possible in an effort to preserve system performance.

6. Conclusions

In this study, a methodology for developing a passive protection spherical cage that enhances drone survivability was presented and discussed. This methodology will aid future designers on the quick and reliable prototyping of spherical-caged systems. Multi-rotors were chosen as the vehicle for this design due to their dense geometry and relative ease of integration with a rotating passive cage that provides defense against foreign obstacles. A dynamic modeling approach that considers the cages dimensions and weight to evaluate the velocity and force in the post-collision was developed. The dynamic model equations including coefficients of restitution, linear momentum, conservation of angular momentum, and Newton's law were methodically formulated to allow use of the known pre-collision parameters to obtain the vehicles post-collision flight properties. A maximum post-collision force of 150 N was derived in the dynamic analysis for a vehicle traveling at 3 m/s in a 1 kg configuration and is used to represent a worse case collision im-
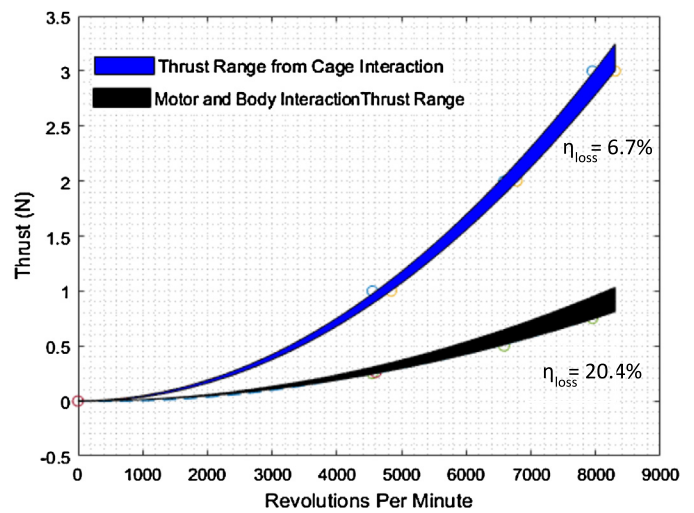
pact in the FEA simulations of the cage deflection and stress. For a 3-ring cage 1 kg configuration that experienced a 3 m/s collision, it was determined that the vehicle will survive but the cage will have damaged portions that need replacement later as the stresses reached 21.2 MPa for the low infill PLA. Simulations of the propellers were also performed to determine the propeller deflection as this constrains the vehicle and cage design as there is a possibility of the propellers striking each other. The greatest deflection was obtained in hovering mode, where a 1 kg configuration vehicle experiences a propeller deflection of 5.5 mm.

The aerodynamic performance of spherical encaged drones was also examined from qualitative and quantitative points of view. Smoke visualization tests in the NMSU wind tunnel indicated that the cage affected drag less than the body. Additional details on the flow disturbance caused by the addition of the cage were studied using PIV where it was found that there is a noticeable velocity deficit up to six cage cross section thicknesses upstream of the cage. At this upstream location, the flow was reduced by 10% compared to the freestream flow. Thrust stand testing provided additional details on thrust optimization of the prototype. The results suggested that to maximize thrust, the body and motor geometry must be optimized to facilitate improved air flow into the motors which improves both flight performance and range to diminish the 20.4% efficiency loss from the body and 6.7% loss from overlapping propellers. A prototype was fabricated, and flight tested to show
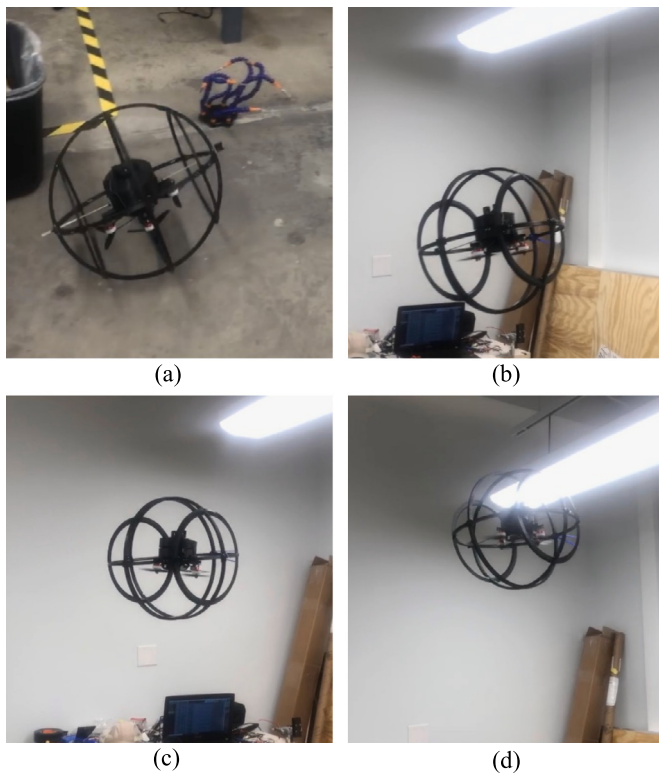
Fig. 18. Flight test of encaged drone prototype through all phases of flight in indoor cluttered environment (a), (b), (c), and (d).

the capability of similar systems for passive protection of multi-rotor drones.

Declaration of competing interest

The authors declare that they have no known competing financial interests or personal relationships that could have appeared to influence the work reported in this paper.

Acknowledgements

References

[1] S. Yoon, H.C. Lee, T.H. Pulliam, Computational analysis of multi-rotor flows, in: Proceedings of the 54th AIAA Aerospace Sciences Meeting, San Diego, CA, USA, January 2016, pp. 4–8.
[2] D. Shukla, N. Hiremath, S. Patel, N. Komerath, Aerodynamic interactions study on low-re-coaxial and quad-rotor configurations, in: ASME International Mechanical Engineering Congress and Exposition, 2017.
[3] W. Zhou, Z. Ning, H. Li, H. Hu, An experimental investigation on rotor-to-rotor interactions of small UAV propellers, in: AIAA Aviation Forum, 2017.
[4] J. Brown, Drone Uses: The Awesome Benefits of Drone Technology, Drone Lab, 2018, [Online]. Available: http://mydronelab.com/blog/drone-uses.html. (Accessed 1 May 2019).
[5] Drone Uses- Applications & Purposes, [Online]. Available, https://mydeardrone.com/uses/, 2019.
[6] Top 12 Non Military Uses for Drone, Air Drone Craze, [Online]. Available: https://airdronecraze.com/drones-action-top-12-non-military-uses/. (Accessed 1 May 2019), 2019.
[7] R. Francis, 10 Unusual Uses for Drone, Explora, [Online]. Available, https://www.bhphotovideo.com/explora/video/tips-and-solutions/10-unusual-uses-drones, 2017.
[8] CBInsights, Research, 24 January 2019, [Online]. Available: https://www.cbinsights.com/research/drone-impact-society-uav/, 24 January 2019.
[9] K. Stelmack, Weaponized police drones and their effect on police use of force, Pittsburgh J. Technol. Law Pol. (2015) 276–292.
[10] K. Nitta, K. Higuchi, Y. Tadokoro, J. Rekimoto, Shepherd pass: ability tuning for augmented sports using ball-shaped quadcopter, in: Proceedings of the 12th International Conference on Advances in Computer Entertainment Technology, 2015.
[11] Hover camera passport self-flying drone w/4K video 13MP P000017, [Online]. Available: https://www.walmart.com/ip/Hover-Camera-Passport-Self-Flying-Drone-w-4K-video-13MP-P000017/412981680?wmlspartner=wlpa&selectedSellerId=711&adid=22222222227278659002&wl0=&wl1=g&wl2=c&wl3=338160793807&wl4=pla-657142771413&wl5=1022560&wl6=&wl7=&wl8=&wl9=pla& [Accessed April 2019].
[12] Kickstarter, Fleye-Your Personal Flying Robot, [Online]. Available: https://www.kickstarter.com/projects/gofleye/fleye-your-personal-flying-robot, 2015, Accessed January 2019].
[13] WTOX, Fleye-your personal flying drone, Youtube, [Online]. Available: https://www.youtube.com/watch?v=Ysy02cpR2rA. [Accessed May 2019].
[14] P.M. Kornatowski, S. Mintchev, D. Floreano, An Origami-Inspired Cargo Drone, IEEE, 2017.
[15] M. Yamada, M. Nakao, Y. Hada, N. Sawasaki, Development and field test of novel two-wheeled UAV for bridge inspections, in: ICUAS, 2017.
[16] Flyability Elios Drone, My Drone, [Online]. Available: https://shop.mydroneservices.com/product/flyability-elios-drone/, 2019, [Accessed February 2019].
[17] S. Mizutani, Y. Okada, C. Salaan, T. Ishii, K. Ohno, S. Tadokoro, Proposal and Experimental Validation of a Design Strategy for a UAV with a Passive Rotating Spherical Shell, IEEE, 2015.
[18] A. Briod, P. Kornatowski, J.C. Zufferey, D. Floreano, A collision-resilient flying robot, J. Field Robot. (2014).
[19] R. Cross, Measurements of the horizontal coefficient of restitution for a super-ball and a tennis ball, Am. J. Phys. (2002).
[20] D. Farbman, C. McCoy, Materials testing of 3D printed ABS and PLA samples to guide mechanical design, in: International Manufacturing Science and Engineering Conference, Blacksburg, ASME, 2016.
[21] F. Dortmun, F. Maschinenbau, Forum for Rapid Technologies, [Online]. Available: https://www.rtejournal.de/ausgabe11/3872, 2014, [Accessed March 2019].
[22] S. Yoon, W.M. Chan, T.H. Pulliam, Computations of torque-balanced coaxial rotor flows, in: AIAA SciTech, 2017.
[23] M.P. Kinzel, J.K. Cornelius, S. Schmitz, J.L. Palacios, J.W. Langelaan, D. Adams, R. Lorenz, An investigation of the behavior of a coaxial rotor in descent and ground effect, in: AIAA SciTech Forum, 2019.
[24] M. Ramasamy, Measurements comparing hover performance of single, coaxial, tandem, and tilt-rotor configurations, in: AHS 69th Annual Forum, 2013.
[25] P. Ventura Diaz, S. Yoon, High-fidelity computational aerodynamics of multi-rotor unmanned aerial vehicles, in: 2018 AIAA Aerospace Sciences Meeting, 2018, p. 1266.
[26] All about multirotor drone FPV propellers, in: GetFPV, 2018, [Online]. Available: https://www.getfpv.com/learn/new-to-fpv/all-about-multirotor-fpv-drone-propellers/. (Accessed 9 March 2013).
[27] J.G.A. van Houten, Large Strain Behaviour of Polycarbonate, TU, Eindhoven, 1994.
[28] A. Simha, M. Tallam, H.N. Shankar, R. Muralishankar, S. Hnln, Adaptive Attitude Control of the Spherical Drone on SO(3), IEEE, 2016.
[29] D. Shukla, N. Komerath, Multirotor drone aerodynamic interaction investigation, Drones 2 (4) (2019) 43, p. 2.
[30] S. Yoon, P. Ventura Diaz, D.D. Boyd, W.M. Chan, C.R. Theodore, Computational aerodynamic modeling of small quadcopter vehicles, in: The 73rd Annual AHS International Forum & Technology Display, Fort Worth, Texas, May 2017.
[31] S. Thibault, D. Holman, S. Garcia, G. Trapani, CFD simulation of a quad-rotor UAV with rotors in motion explicitly modeled using an LBM approach with adaptive refinement, in: AIAA Conference 2017, 2017.
[32] J.J. Chiew, M.J. Afosmis, Efficient simulation of multi-rotor vehicles with low Reynolds number propellers, in: AIAA Aviation Forum, 2018.
[33] B. Theys, G. Dimitriadis, P. Hendrick, J. De Schutter, Influence of propeller configuration on propulsion system efficiency of multi-rotor Unmanned Aerial Vehicles, in: International Conference on Unmanned Aircraft Systems, 2016.
[34] Y. Zheng, S. Yang, X. Liu, J. Wang, T. Norton, J. Chen, Y. Tan, The computational fluid dynamic modeling of downwash flow field for a six-rotor UAV, Front. Agric. Sci. Eng. 5 (2018).